

# DoseDiff: Distance-aware Diffusion Model for Dose Prediction in Radiotherapy

Yiwen Zhang<sup>1,2\*</sup>, Chuanpu Li<sup>1,2\*</sup>, Liming Zhong<sup>1,2</sup>, Zeli Chen<sup>1,2</sup>, Wei Yang<sup>1,2†</sup>, and Xuetao Wang<sup>3†</sup>

<sup>1</sup>School of Biomedical Engineering, Southern Medical University, Guangzhou 510515, China

<sup>2</sup>Guangdong Provincial Key Laboratory of Medical Image Processing, Guangzhou 510515, China

<sup>3</sup>Department of Radiation Therapy, The Second Affiliated Hospital, Guangzhou University of Chinese Medicine, Guangzhou 510006, China

**Abstract:** Treatment planning is a critical component of the radiotherapy workflow, typically carried out by a medical physicist using a time-consuming trial-and-error manner. Previous studies have proposed knowledge-based or deep learning-based methods for predicting dose distribution maps to assist medical physicists in improving the efficiency of treatment planning. However, these dose prediction methods usually lack the effective utilization of distance information between surrounding tissues and targets or organs-at-risk (OARs). Moreover, they are poor in maintaining the distribution characteristics of ray paths in the predicted dose distribution maps, resulting in a loss of valuable information obtained by medical physicists. In this paper, we propose a distance-aware diffusion model (DoseDiff) for precise prediction of dose distribution. We define dose prediction as a sequence of denoising steps, wherein the predicted dose distribution map is generated with the conditions of the CT image and signed distance maps (SDMs). The SDMs are obtained by a distance transformation from the masks of targets or OARs, which provide the distance information from each pixel in the image to the outline of the targets or OARs. Besides, we propose a multi-encoder and multi-scale fusion network (MMFNet) that incorporates a multi-scale fusion and a transformer-based fusion module to enhance information fusion between the CT image and SDMs at the feature level. Our model was evaluated on two datasets collected from patients with breast cancer and nasopharyngeal cancer, respectively. The results demonstrate that our DoseDiff outperforms the state-of-the-art dose prediction methods in terms of both quantitative and visual quality.

**Keywords:** Deep learning, Diffusion model, Dose prediction, Radiotherapy, Signed distance map.

## 1 Introduction

Radiation therapy (RT) is an essential cancer treatment modality, with approximately 50% of cancer patients receiving it during their course of illness and contributing to around 40% of curative treatment [1, 2]. In the current RT workflow, treatment planning plays an important role as it determines the optimal radiation dose, technique, and schedule to target cancer while minimizing exposure to healthy tissue,

---

\* Yiwen Zhang and Chuanpu Li are co-first authors.

† Corresponding authors: Xuetao Wang (wangxuetao0625@126.com); Wei Yang (weiyanggm@gmail.com).

aiming to maximize effectiveness and minimize side effects. Clinically, a medical physicist typically spends hours adjusting a set of hyper-parameters and weightings in a trial-and-error manner to ensure that the RT plan can achieve the desired treatment effect, which is time-consuming and labor-intensive [3, 4]. If an appropriate dose distribution map is obtained in advance, the medical physicist will be able to use the dose distribution map as a reference to finishing the RT planning with fewer hyper-parameter adjustments [5, 6]. Therefore, dose prediction is of great value in enhancing efficiency and streamlining the workflow in RT.

Various approaches have been proposed for dose prediction in RT. Knowledge-based planning (KBP) provides a traditional paradigm for dose prediction that leverages planning information from historical patients to predict the dosimetry for a new patient [7, 8]. Initially, some handcrafted features related to dosimetry are directly used to match historical patients with new patients, e.g., overlap volume histogram (OVH) [9], distance-to-target histogram (DTH) [10], and planning volume shapes [11]. With the development of machine learning technology, support vector regression, random forests, and gradient boosting have been used to find more effective features [12-14]. However, these KBP-based methods typically concentrate on predicting dosimetric endpoints (DEs) or dose volume histograms (DVHs), which are dosimetric-related statistical indicators and lack spatial information [5]. Furthermore, the accuracy of methods that rely on traditional feature extraction often falls short of expectations.

Deep learning is another currently popular approach for dose prediction [5, 6, 15-24]. With its powerful feature extraction and analysis capabilities, the deep learning model is able to learn the mapping relationship from computerized tomography (CT) images and region-of-interest (ROI) masks, i.e., targets and organs-at-risk (OARs), to dose distribution maps. Nguyen et al. [21] and Fan et al. [16] first involved the utilization of a 2D convolutional neural network (CNN) to predict dose distribution slice by slice, with the ultimate objective of achieving 3D dose prediction. To make full use of spatial information, Kearney et al. [17] proposed the DoseNet, a modified 3D UNet, for volumetric dose prediction. Recent research focuses on constructing more effective loss functions to improve the accuracy of dose prediction, e.g., adversarial loss [18] and ROI-weighted loss [5].

Most existing deep learning-based dose prediction methods directly use CT images and ROI masks as model inputs, which rarely exploit distance information between surrounding tissues and the targets or OARs. In RT planning, distance information is important as the relative positions of ROIs determine their mutual influence, e.g., the dose levels of the tissues close to the targets are relatively large and that of the tissues near the OARs are relatively small [23, 25]. Although CNNs are capable of implicitly learning the distance relationship among ROIs from masks, most of deep learning-based methods use a slice-based or patch-based training strategy due to memory constraints, which results in their inability to leverage useful information from images of mask when the slice or patch contains little or no ROI. To the best of our knowledge, only Kontaxis et al. [19] and Yue et al. [23] have introduced distance information into the neural networks through distance maps. However, the method proposed by Kontaxis et al. [19] requires knowledge of the parameters of beamlets to calculate the distance

map from the central beamline, which is often not practical in a clinical setting. Yue et al. [23] utilized ROI masks for distance map calculation and proposed a normalization technique to rescale the numerical range of the distance map for network training, but their distance map only considers pixel distance in matrix space, rather than real-world physical distance, and has a limited dynamic range. In addition, they simply concatenated the distance maps and CT images as the network inputs, which restricts the potential performance of their model. Various studies have shown that feature-level fusion is more capable of capturing complex relationships among different modalities compared to input-level fusion [26-28].

Ensuring the authenticity and feasibility of the predicted dose distribution map is also a challenge, e.g., it involves ensuring that the radiation paths in the map adhere to straight-line propagation and that the predicted cumulative dose distribution can be achieved within an acceptable number of treatment fields. However, the existing deep learning-based dose prediction methods typically only learn the mapping from input to output images, which cannot fully capture the prior data distribution of real dose distribution map. As a result, their predicted dose distribution maps appear excessively smooth and distort ray path characteristics. Some studies have adopted the frameworks based on generative adversarial network (GAN) to enhance the realism of the predicted dose distribution map [5, 18], but GANs can be challenging to train and often drop modes in the output distribution [29-31]. Recently, the diffusion model [32, 33] has attracted attention as a powerful generative model, capable of modeling complex image distribution. diffusion model has been shown to provide superior image sampling quality and more stable training compared to the GANs [34]. The conditional diffusion model introduces conditional information to guide the model in generating specific images. Some researchers have applied conditional diffusion model to various image-to-image translation tasks and achieved the SOTA results, e.g., image inpainting [35], colorization [31], and super-resolution [36]. Different from the previous method of learning pixel mapping between input and output, conditional diffusion model can learn the data distribution from training images and sample the images that best match the given conditions from the distribution. Besides, conditional diffusion model partitions image-to-image generation into a sequence of denoising steps, which typically recover the general outline initially and then produce details. This can be considered as a recursive image generation method, which has been proven to be effective by previous studies [37-39]. Despite these superiorities, further exploration is required to fully realize the potential of the diffusion model in the task of predicting dose distribution in radiotherapy.

In this paper, we propose a novel distance-aware conditional diffusion model for dose prediction named DoseDiff, which takes CT images and signed distance maps (SDMs) as conditions to accurately generate dose distribution maps. Based on the conditional diffusion model mechanism, we define dose prediction as a sequence of denoising steps, wherein the predicted dose distribution maps are generated from Gaussian noise images with the guide of conditions. The SDMs are obtained by performing a distance transform on the masks, which indicates the distance of each voxel in the image from the contours of the ROIs in 3D space. Unlike Yue et al. [23],

who simply combined CT images and distance maps through channel concatenation at the input, we propose a Multi-encoder and Multi-scale Fusion Network (MMFNet) to enhance information fusion at the feature level. We design independent encoders for CT images and SDMs respectively and perform information fusion on feature maps of multiple scales. Also, a fusion module based on transformer [40, 41] technology is proposed in the MMFNet to further fuse global information.

The main contributions of this paper are summarized as follows.

- We propose DoseDiff, a first conditional diffusion model designed for dose prediction in radiotherapy. Besides, we convert the masks into the SDMs in 3D physical space to facilitate the model's perception of the distance relationship between surrounding tissues and the targets or OARs.
- We propose MMFNet to more effectively extract and fuse features from CT images and SDMs. A transformer-based fusion module in MMFNet is used to further capture global information.
- We evaluate our model using data from breast cancer and nasopharyngeal carcinoma (NPC) patients undergoing radiotherapy. The experiments show that our method outperforms the SOTA dose prediction methods on both datasets.

## 2 Method

### 2.1 Background

The conditional diffusion model is a class of conditional generative methods aimed at transforming a Gaussian distribution to the empirical data distribution [33, 42, 43], which usually involves two processes in opposite directions: forward (diffusion) process and reverse process. We denote  $x$  and  $y_0$  are the condition and target domain image, respectively. The forward process aims to collapse the target image distribution  $p(y_0)$  to a standard Gaussian distribution  $\mathcal{N}(0, I)$  by gradually adding Gaussian noise of varying scales to the target image:

$$q(y_t | y_{t-1}) = \mathcal{N}(y_t; \sqrt{\alpha_t} y_{t-1}, (1 - \alpha_t)I); \quad (1)$$

$$q(y_t | y_0) = \mathcal{N}(y_t; \sqrt{\bar{\alpha}_t} y_0, (1 - \bar{\alpha}_t)I), \quad (2)$$

where  $t \in [1, T]$  is the timestep and  $T$  denotes the total diffusion steps. The scale of the added Gaussian noise is determined by a set of hyper-parameters  $\alpha_t$  that change concerning  $t$ , and  $\bar{\alpha}_t = \prod_{s=1}^t \alpha_s$ . With the theoretical assumption of the diffusion model, when  $T$  is sufficiently large,  $p(y_T)$  can be approximated as a standard Gaussian distribution [42, 44].

The target image is generated by fitting other distributions that are parameterized by  $\theta$  in the reverse process:

$$p_\theta(y_{t-1} | y_t) = \mathcal{N}(y_{t-1}; \mu_\theta(y_t, x, t), (1 - \alpha_t)I), \quad (3)$$

where  $\mu_\theta(y_t, x, t)$  can be parameterized by a neural network  $\epsilon_\theta(y_t, x, t)$ . The objective of training the neural network is to minimize the variational upper bound of the negative log-likelihood:

$$\mathcal{L}_\theta = \mathbb{E}_{y_0, x, t, \epsilon} \|\epsilon - \epsilon_\theta(y_t, x, t)\|, \quad (4)$$

where  $\epsilon \sim \mathcal{N}(0, I)$ .

## 2.2 DoseDiff

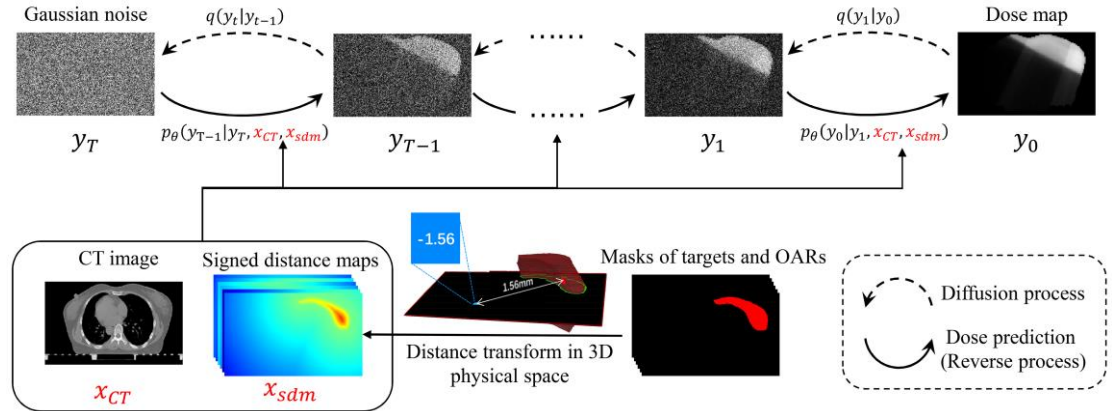


**Fig. 1.** The overall workflow of our DoseDiff.

Different from the previous methods, conditional diffusion model possesses the capability to model the data distribution, which is beneficial for the model to perceive the dose distribution characteristics in the real dose distribution map. Furthermore, conditional diffusion model exhibits more stable training and yields higher image quality compared to GAN-based methods. Therefore, we propose the DoseDiff for dose prediction, as shown in Fig. 1. The DoseDiff is essentially a conditional diffusion model conditioned by CT images and SDMs, which considers dose prediction as a sequence of denoising steps, i.e., reverse process. To adapt the two conditional terms, we redefine the neural network as  $\epsilon_\theta(y_t, x_{CT}, x_{sdm}, t)$  and accordingly modify the reverse process and objective function outlined in Eqs. (3) and (4):

$$p_\theta(y_{t-1}|y_t) = \mathcal{N}(y_t; \mu_\theta(y_t, x_{CT}, x_{sdm}, t), (1 - \alpha_t)I), \quad (5)$$

$$\mathcal{L}_\theta = \mathbb{E}_{y_0, x_{CT}, x_{sdm}, \epsilon} \|\epsilon - \epsilon_\theta(y_t, x_{CT}, x_{sdm}, t)\|, \quad (6)$$

where  $x_{CT}$  and  $x_{sdm}$  are CT image and SDM, respectively.

The conditional diffusion model assumes that the reverse process is a Markov chain and diffusion step  $T$  should be sufficiently large. Therefore, the inference of DoseDiff consumes a significant computational time. To reduce the inference time, we adopt the accelerated generation technology of the denoising diffusion implicit model (DDIM) [45]. Based on the non-Markovian hypothesis, the DDIM allows a reduced number of sampling steps, less than  $T$ , in the inverse process. Furthermore, the implementation of DDIM solely requires modifications to the sampling technique of the inverse process, without impacting the training and forward process. Let  $\tau$  represent a sub-sequence of  $[1, \dots, T]$  of length  $S$  with  $\tau_S = T$ , the accelerated reverse process of our DoseDiff can be expressed as:

$$\begin{aligned}
p_\theta(y_{\tau_{i-1}}|y_{\tau_i}) &= \mathcal{N}\left(\sqrt{\bar{\alpha}_{\tau_{i-1}}}\hat{y}_0^{(\tau_i)} + \sqrt{\bar{\alpha}_{\tau_i} - \bar{\alpha}_{\tau_{i-1}}}\right. \\
&\quad \left.\cdot \frac{y_{\tau_i} - \sqrt{\bar{\alpha}_{\tau_i}}\hat{y}_0^{(\tau_i)}}{\sqrt{1 - \bar{\alpha}_{\tau_i}}}, (1 - \alpha_t)I\right) \text{ if } i \in [S], i > 1 \\
p_\theta(y_0|y_t) &= \mathcal{N}\left(\hat{y}_0^{(t)}, (1 - \alpha_t)I\right) \text{ otherwise,}
\end{aligned}
\tag{7}$$

where  $\hat{y}_0^{(t)} = (y_t - \sqrt{1 - \bar{\alpha}_t}\epsilon_\theta(y_t, x_{CT}, x_{sdm}, t))/\sqrt{\bar{\alpha}_t}$ .

### 2.3 Signed distance map

Most previous dose prediction methods directly use masks to provide location and distance information of ROIs. A limitation of using the masks is that the current slice-based and patch-based CNN training strategies cannot guarantee that all foreground regions in the images of mask are completely included in the sampled images. Moreover, although CNNs are capable of implicitly learning the distance relationship among ROIs from mask images, their convolution kernels can only extract local features, which makes CNNs may struggle to perceive long-range distance relationships. On the contrary, the distance map calculates the distance from each voxel to the contour of the ROI in the 3D space of the image. The distance image value itself is capable of conveying distance information, regardless of the limitations imposed by the incomplete sampling of the image or the limited receptive field of CNNs. The SDM identifies whether a voxel is inside or outside the ROI by using a sign.

Let  $M_k$  denote the mask image, where  $k \in [1, K]$  and  $K$  is the total number of targets and OARs. We denote  $M_k^{in}$ ,  $M_k^{out}$ ,  $\partial M_k$  are inside, outside, and boundary of the ROI, respectively. The SDM in matrix space (MSDM) is defined as:

$$x_k^{msdm} = \begin{cases} \inf_{j \in \partial M_k} \|i - j\|_2, i \in M_k^{in} \\ 0, i \in \partial M_k \\ -\inf_{j \in \partial M_k} \|i - j\|_2, i \in M_k^{out} \end{cases},
\tag{9}$$

where  $\|i - j\|_2$  is the Euclidian distance between voxels  $i$  and  $j$ . However, due to the inconsistent voxel resolution, MSDM values are not comparable between different images and have no practical connotation. Therefore, we consider spacing as a factor when calculating the SDM, transforming the MSDM from matrix space to physical space (PSDM):  $x_k^{psdm} = x_k^{msdm} \cdot spacing$ . Finally, the input SDM  $x_{sdm}$  of the neural network  $\epsilon_\theta(y_t, x_{CT}, x_{sdm}, t)$  is a collection of the SDMs of all ROIs:

$$x_{sdm} = \{x_1^{psdm}, x_2^{psdm}, \dots, x_{K-1}^{psdm}, x_K^{psdm}\}.
\tag{10}$$

### 2.4 MMFNet

The conditions in our DoseDiff contain multimodal images, i.e., CT image and SDM. To effectively extract and fuse the features of them, we propose MMFNet for  $\epsilon_\theta$ ,

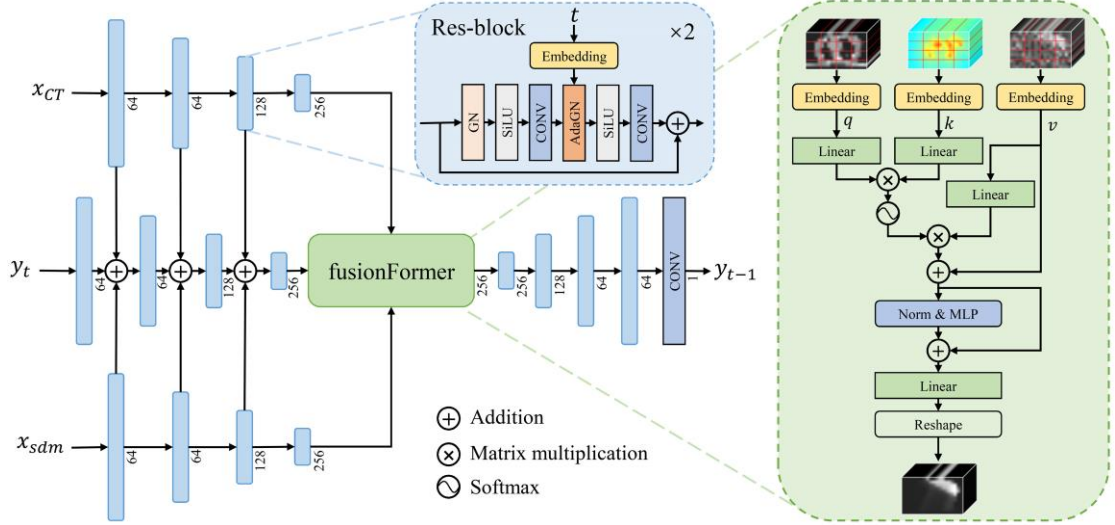


**Fig. 2.** Architecture of our MMFNet for dose prediction.

as shown in Fig. 2. The MMFNet adopts UNet architecture with multiple encoders that the three encoders are used to extract the features of  $x_{CT}$ ,  $x_{sdm}$ , and  $y_t$ , respectively. The encoder part accomplishes the multi-scale information fusion by summing feature maps of the same resolution from three inputs at every level. Our encoders and decoder are implemented in the same way as that of [34], which involves four down-sampling or up-sampling operations. Each level of encoders and decoder contains two residual blocks (Res-blocks), and each Res-block is composed of one group normalization (GN) layer, two sigmoid linear units (SiLUs), two  $3 \times 3$  convolution layers, one adaptive GN (AdaGN) layer, and one residual connection. Similarly, the timestep  $t$  is embedded in each Res-block through AdaGN, which is defined as [34]:

$$\text{AdaGN}(f, e_t) = e_t^s \text{GN}(f) + e_t^b, \quad (11)$$

where  $f$  is the input feature map and  $e_t = [e_t^s, e_t^b]$  is obtained from a linear projection of the timestep  $t$ .

We proposed a transformer-based fusion module, fusionFormer, further global information fusion. Different from the convolution layer to extract local features, transformer [40, 41] adopts an attention mechanism to capture global context information. A currently popular approach to enhance model performance is to combine the strengths of CNN and transformer for local and global feature extraction [46-48]. To minimize memory cost, the fusionFormer is added to the path at the lowest resolution level. In fusionFormer, the feature maps of  $x_{CT}$ ,  $x_{sdm}$ , and  $y_t$  are partitioned into non-overlapping patches, i.e., the channels remain unchanged while evenly slicing along the length and height dimensions, and then transformed into three fundamental components of the attention using an embedded layer consisting of linear and normalization layers: query ( $f_q$ ), key ( $f_k$ ), and value ( $f_v$ ). As both  $x_{CT}$  and  $x_{sdm}$  are conditions, we use their feature maps as query and key to calculate attention matrix. The attention matrix is then used to weight the feature map of the noisy dose distribution map, enabling conditional guidance. The attention block in Transformer can be expressed as follows:

$$f_{att} = \text{Softmax}(\beta(f_q) \times \gamma(f_k)^T) \times \delta(f_v) + \delta(f_v), \quad (12)$$

where  $\beta(\cdot)$ ,  $\gamma(\cdot)$ , and  $\delta(\cdot)$  are linear operation. Then a feed-forward block is used for

the nonlinear transformation of features:

$$f_{ffb} = \text{MLP}(\text{LN}(f_{att})) + f_{att}, \quad (13)$$

where  $\text{MLP}(\cdot)$  is a multi-layer perceptron consisting of two linear layers and a nonlinear activation function and  $\text{LN}(\cdot)$  is layer normalization. Lastly, a linear layer is applied to adjust the dimensionality of the feature vector to the original size, which is then reshaped to the shape the same as the input feature maps.

## 2.5 Implementation details

Our network implementation is based on PyTorch<sup>‡</sup>, and the codes ran on a server with two RTX 2080Ti GPUs. Following [42], we set total diffusion steps  $T$  to 1000 and the forward process variances  $\alpha_t$  to constants decreasing linearly from  $\alpha_1 = 0.9999$  to  $\alpha_T = 0.08$ . To ensure the model's input value falls within a suitable range, we set the distance unit for the PSDM to decimeters. We used the AdamW [49] optimizer with a step-decay learning rate to train our model for one million iterations. The initial learning rate and batch size were 0.0001 and 8, respectively. Some simple online data augmentation operators, including random flipping, rotating, and zooming, were used on the training set to improve the generalization capacity of the model. To reduce the inference time, we set the reduced generation step  $S$  in DDIM to 8.

## 3 Experiment

### 3.1 Datasets and preprocessing

The breast cancer and NPC datasets were constructed by collecting the data of patients receiving RT from a hospital (Guangdong Provincial Hospital of Traditional Chinese Medicine in China) from 2016 to 2020. The patients in the breast cancer dataset underwent postoperative RT following breast-conserving surgery, while the patients in the NPC dataset received RT for primary lesions. The CT volumes were obtained using a Siemens Sensation Open (Siemens Healthcare, Forchheim, Germany) scanner. Their radiotherapy plans were received from a treatment planning system (Philips, Pinnacle<sup>3</sup>, Netherlands). All the targets and OARs are delineated by experienced oncologists and all the plans are clinically approved. The details of breast cancer and NPC datasets are described as follows.

**Breast cancer dataset:** The breast cancer dataset consists of 119 patients. The in-plane pixel spacings of the CT images range from 0.77 to 0.97 mm with an average of 0.95 mm and slice thicknesses are all 5.0 mm. The in-plane resolutions are  $512 \times 512$  and the number of slices ranges from 50 to 129. We used a binary body mask to exclude the unnecessary background of each image and all the images were cropped by the minimal external cube of the body masks and then resized to  $320 \times 192$  in-plane. The target areas of tumor bed (TB) and clinical target volume (CTV), and the OARs of the heart, spinal cord, and left and right lungs were included in our experiments.

**NPC dataset:** The NPC dataset consists of 139 patients. The in-plane pixel spacings of the CT images range from 0.75 to 0.97 mm with an average of 0.95 mm

---

<sup>‡</sup> <https://pytorch.org/>

and slice thicknesses are 3.0 mm. The in-plane resolutions are  $512 \times 512$  and the number of slices ranges from 69 to 176. All images were also masked and cropped by body masks but then resized to  $448 \times 224$  in-plane. The target areas include gross tumor volume (GTV) and planning target volume (PTV), and the OARs include eyes, optic nerve, temporal lobe, brain stem, parotid gland, mandible, and spinal cord.

The intensity ranges of CT images and dose distribution maps was set to  $[-1000, 1500]$  HU and  $[0, 75]$  Gy, respectively. Both were uniformly and linearly normalized to  $[-1, 1]$  for training. Both datasets were split into training, validation, and test sets using a patient-wise ratio of 7:1:2, which were utilized for model training, model selection, and performance evaluation, respectively.

### 3.2 Evaluation metrics

To evaluate the model performance quantitatively, we used both common image similarity metrics and dosimetry-related metrics. The used common image similarity metrics include the mean absolute error (MAE), the structural similarity index measurement (SSIM), and the signal-to-noise ratio (PSNR):

$$\text{MAE}(u, v) = \frac{1}{N} \sum_{i=1}^N |u_i - v_i|, \quad (14)$$

$$\text{SSIM}(u, v) = \frac{(2\mu_u\mu_v + c_1)(2\sigma_{uv} + c_2)}{(\mu_u^2 + \mu_v^2 + c_1)(\sigma_u^2 + \sigma_v^2 + c_2)}, \quad (15)$$

$$\text{PSNR}(u, v) = 10\log_{10} \left( \frac{c_{range}^2}{\frac{1}{N} \sum_{i=1}^N (u_i - v_i)^2} \right), \quad (16)$$

where  $N$  is the total number of voxels;  $u_i$  and  $v_i$  are the  $i^{th}$  voxel value in volumes  $u$  and  $v$ , respectively. The symbols  $\mu_u$ ,  $\mu_v$ ,  $\sigma_u$ ,  $\sigma_v$ , and  $\sigma_{uv}$  denote local mean, variance, and covariance of volumes  $u$  and  $v$ .  $c_{range}$  denotes the distance between minimum and maximum possible values of input images, which is set to 75 in our experiments. Following [50],  $c_1 = (0.01c_{range})^2$  and  $c_2 = (0.03c_{range})^2$  are constants to stabilize the division. For accurate performance evaluation, these three metrics were computed within the body masks to eliminate the influence of the background.

The dosimetry-related metrics include  $\Delta D_V$  and  $\Delta V_D$ . The symbol  $\Delta$  denotes the absolute error of the dosimetric metrics between the predicted and ground-truth dose distribution maps.  $D_V$  denotes the dose received by  $V\%$  of the volume of the ROIs.  $D_{min}$ ,  $D_{mean}$ , and  $D_{max}$  are also considered as members of  $D_V$ , indicating the minimum, average and maximum dose in the ROI, respectively. For the treatment targets,  $V_D$  is the volume percentage of the target region receiving  $D\%$  of the prescribed dose; for OARs,  $V_D$  is the volume percentage of the ROI receiving  $V$  Gy dose. In clinical practice, different indicators are considered for different ROIs. Therefore, we assigned appropriate evaluation metrics for different ROIs in the two datasets. In the breast cancer dataset, we used  $\Delta D_{95}$  and  $\Delta V_{95}$  for TB and CTV;

$\Delta D_{mean}$  and  $\Delta V_{30}$  for the heart;  $\Delta D_{mean}$  and  $\Delta V_{20}$  for ipsilateral lung; and  $\Delta D_{max}$  for the spinal cord. In the NPC dataset, we used  $\Delta D_{95}$  and  $\Delta V_{95}$  for GTV and PTV;  $\Delta D_{max}$  for eyes, optic nerve, temporal lobe, brain stem, and spinal cord;  $\Delta D_{mean}$  and  $\Delta V_{30}$  for parotid gland; and  $\Delta D_{min}$  for the mandible. To facilitate model comparison and selection, we defined the mean of  $\Delta D_V$  and  $\Delta V_D$  for all ROIs as “dose score” and “volume score”, respectively. The dose-volume histogram (DVH) was used for a comprehensive comparison of the differences between the predicted results of different methods and the real dose distribution.

### 3.3 Ablation studies for DoseDiff

We conducted ablation studies to quantitatively validate the contribution of each term in our DoseDiff. Specifically, we sequentially added PSDM input, multi-scale fusion (MS), and fusionFormer module (FF) into the baseline conditional diffusion model, which initially only used CT images as input. Moreover, we added the proposed elements to the baseline UNet model to further prove their effectiveness. As shown in Table 1, the results show that the introduction of PSDM results in the most significant performance improvement. While multi-scale fusion has shown limited improvement in the common image similarity metrics, it has significantly enhanced the dosimetric metrics. Compared to the conditional diffusion model baseline, the DoseDiff improved by 1.747Gy in MAE, 0.093 in SSIM, 7.848dB in RSNR, 9.693Gy in dose score, and 18.491% in volume score. Furthermore, the experimental results demonstrate that the proposed elements are effective in both the UNet and conditional diffusion model frameworks, with conditional diffusion model generally outperforming UNet in terms of performance. The ablation experiments have indicated that incorporating distance information and enhancing the fusion strategy can be beneficial in achieving accurate dose distribution prediction for deep-learning models.

**Table 1** Results of ablation studies for DoseDiff on the breast cancer dataset.

UNet	Diffusion model	PSDM	MS	FF	MAE (Gy)↓	SSIM↑	PSNR (dB)↑	Dose score (Gy)↓	Volume score (%)↓
√					3.416±1.741	0.797±0.077	19.675±4.175	11.206±7.456	18.910±9.909
√	√				1.438±0.224	0.896±0.032	26.662±1.240	1.880±0.611	11.301±8.167
√	√	√			1.420±0.211	0.890±0.034	26.710±1.140	1.150±0.333	1.718±1.357
√	√	√	√		<b>1.221±0.241</b>	<b>0.913±0.030</b>	<b>27.813±1.649</b>	<b>1.047±0.438</b>	<b>1.256±0.740</b>
	√				2.937±1.132	0.807±0.052	20.27±3.134	10.391±6.376	19.413±7.791
	√	√			1.223±0.206	0.903±0.209	27.710±1.539	1.575±0.440	7.031±7.549
	√	√	√		1.201±0.208	<b>0.906±0.028</b>	27.700±1.485	0.848±0.233	1.138±0.563
	√	√	√	√	<b>1.190±0.227</b>	0.900±0.028	<b>28.118±1.699</b>	<b>0.698±0.131</b>	<b>0.922±0.296</b>

### 3.4 Performance of PSDM

To verify the benefit of the proposed PSDM, we compare the DoseDiffs with different distance information input, including mask, transformed signed boundary distance map (TSBDM) [23], MSDM, and PSDM. Note that we shrunk all MSDM values by a factor of 100 to stabilize the training. Table 2 shows the quantitative

comparison results that PSDM achieves the best performance. The visual comparison of the mask, TSBDM, MSDM, and PSDM on the ROIs of breast cancer is presented in Fig. 3. As shown, the distance maps can provide more distinct and effective distance information than the mask images. However, the voxel-wise transformation in TSBDM quickly zeros out the pixels far from the contour, rendering many background pixels ineffective. In addition, the dynamic change of distance is not obvious in TSBDM. PSDM converts the image distance to the real-world distance, which enables the model to extract the distance map information in different volumes under a consistent measure. Also, PSDM is more practical than MSDM in the clinic, for example, MSDM equates the in-plane and inter-slice pixel distance, but the slice thickness of CT images is usually larger than the in-plane spacing.

**Table 2** Quantitative comparison of the DoseDiffs with original mask, TSBDM, MSDM, and PSDM input, respectively.

Input	MAE (Gy)↓	SSIM↑	PSNR (dB)↑	Dose score (Gy)↓	Volume score (%)↓
Mask	1.536±0.244	0.859±0.031	25.632±1.271	0.856±0.238	<b>0.921±0.372</b>
TSBDM	1.287±0.219	0.859±0.029	28.099±1.673	0.788±0.238	0.928±0.304
MSDM	1.248±0.214	0.878±0.028	28.042±1.632	0.705±0.181	0.928±0.300
PSDM	<b>1.190±0.227</b>	<b>0.900±0.028</b>	<b>28.118±1.699</b>	<b>0.698±0.131</b>	0.922±0.296

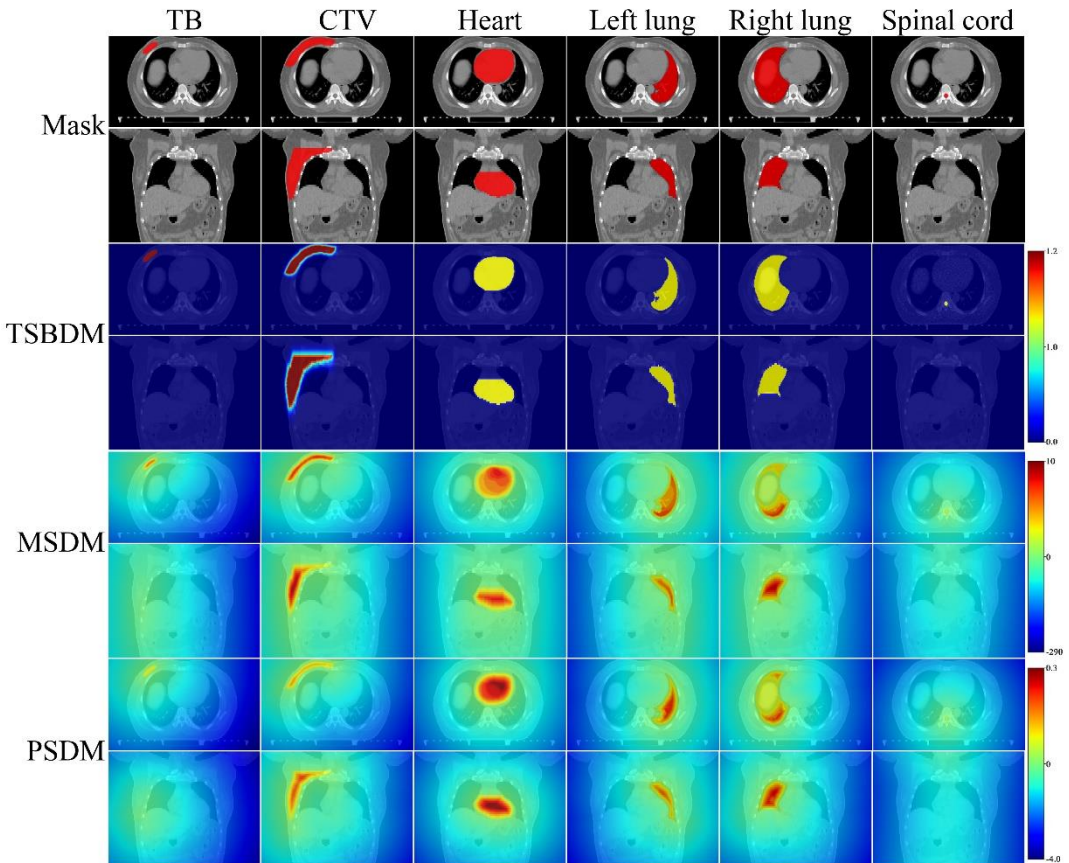


**Fig. 3.** Visual comparison of the mask, TSBDM, MSDM, and PSDM on the ROIs of breast cancer.

### 3.5 Trade-off between performance and inference speed

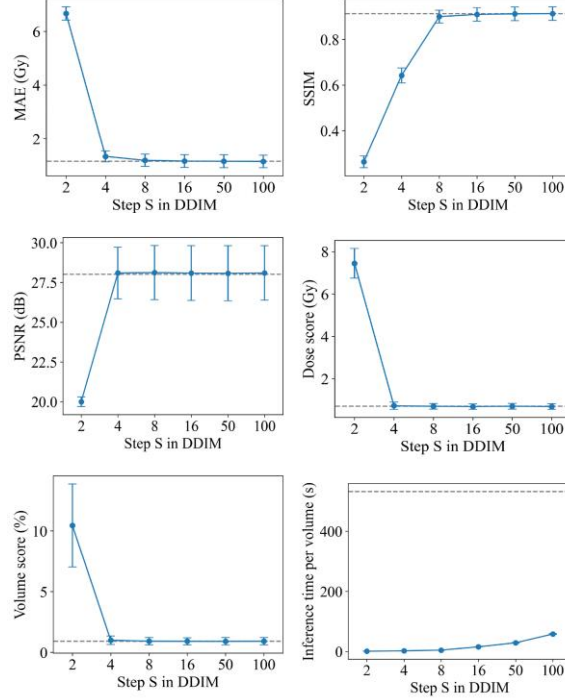


**Fig. 4.** Performance and inference time of different generation steps based on DDIM reverse process.

The gray dotted lines indicate the metrics of DoseDiff without DDIM ( $T = 1000$ ).

In diffusion model, the generative process is defined as the reverse of a particular Markovian diffusion process. Consequently, the generation of the image necessitates a complete sequence of sampling, which is time-consuming. The DDIM converts the Markovian diffusion process in diffusion model into a non-Markovian diffusion process that allows us to trade off computation for sample quality. Based on the DDIM, we conducted a comparison of the performance and inference time of DoseDiff across varying generation steps. As shown in Fig. 4, the experimental results show that the performance of the model improves with more generation steps, but stabilizes after 8 steps. The inference time is approximately proportional to the number of generation steps. To trade off performance and inference time, we suggest setting the generation step to 8 in the DDIM reverse process and our subsequent experiments all adopt this setting.

### 3.6 Comparison with SOTA

To demonstrate the superiority of our method, we conducted a comparison between the DoseDiff and several state-of-the-art dose prediction methods, which included the 2D models of DeeplapV3+ [6] and MCGAN [5], as well as the 3D models of DoseNet [17], DoseGAN [18], and distance-guided deep learning (DGDL) [23]. Among these compared methods, DGDL differs in its use of TSBDM distance maps as input, whereas the other methods utilize mask images. We conducted both quantitative and visual comparisons on breast cancer and NPC datasets.

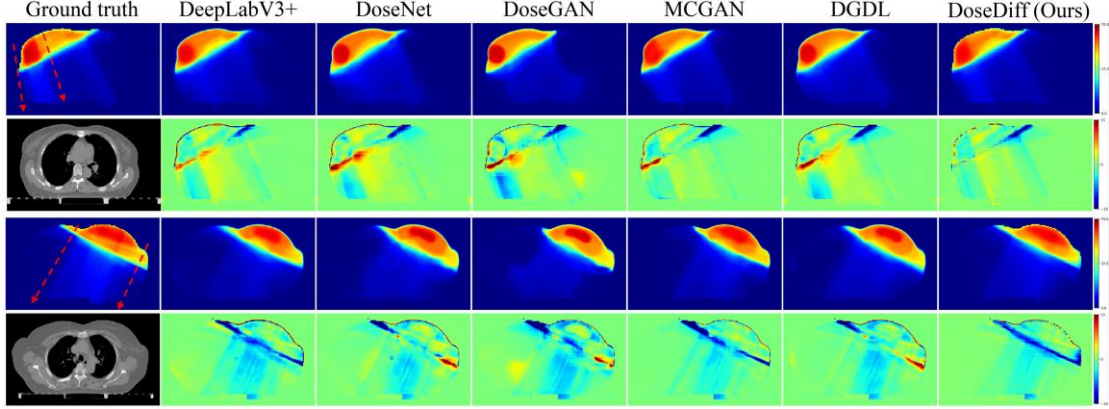


**Fig. 5.** Visual comparison of predicted dose distribution maps from different methods on the breast cancer dataset. The red dashed arrows represent the estimated input directions of certain rays identified from the real dose distribution maps.

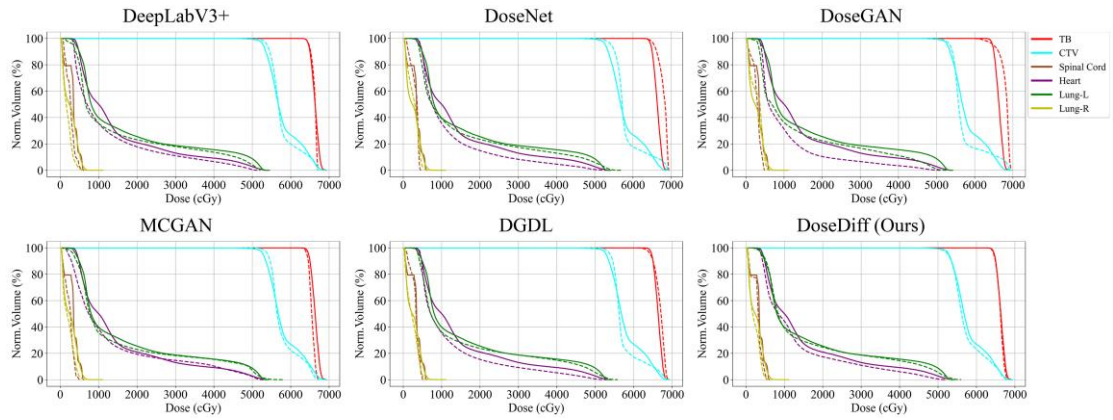


**Fig. 6.** The dose-volume histograms (DVHs) of the dose distribution maps predicted by the different methods on a testing breast cancer patient. The solid line represents the ground-truth DVH, while the dotted line represents the DVH of the predicted dose distribution map.

**Comparison on breast cancer dataset:** Table 3 illustrates the common image similarity metrics and detailed dosimetry-related metrics of all compared methods on the breast cancer dataset. The results show that our method obtains stable top performance in most evaluation metrics. Fig. 5 shows predicted dose distribution maps from different methods, as well as the difference between their dose distribution maps and the ground truths. We can observe that the dose distribution predicted by our method is closer to the real dose distribution. Specifically, it can learn a clear path of the light ray that reflects the fundamental properties of straight-line propagation, which is beneficial for medical physicists to obtain precise parameters, such as the number of radiation fields and the incident angle, from the predicted dose distribution map. Furthermore, Fig. 6 presents the DVHs of the dose distribution maps predicted by the compared methods, allowing for a comprehensive comparison of the dose distributions. We also observe that the DVH curve of the dose distribution map predicted by our method is more similar to the ground-truth curve.

**Table 3** Quantitative comparison with SOTA methods for dose prediction on breast cancer dataset.

ROI	Metrics	DeepLabV3+	DoseNet	DoseGAN	MCGAN	DGDL	DoseDiff (Ours)
Body	MAE(Gy)↓	1.602±0.307	1.385±0.256	1.706±0.268	1.510±0.268	1.330±0.242	<b>1.076±0.232</b>
	SSIM↑	0.851±0.034	0.857±0.030	0.821±0.031	0.858±0.026	0.880±0.027	<b>0.913±0.024</b>
	PSNR(dB)↑	25.861±1.367	28.555±1.452	26.121±1.312	25.287±1.305	28.425±1.376	<b>28.887±1.481</b>
TB	$\Delta D_{95}(\text{Gy})\downarrow$	0.794±0.737	<b>0.623±0.416</b>	0.854±0.759	1.204±0.669	1.029±0.657	1.035±0.602
	$\Delta V_{95}(\%) \downarrow$	0.098±0.254	<b>0.029±0.074</b>	0.503±0.528	0.037±0.061	0.185±0.327	0.084±0.194
CTV	$\Delta D_{95}(\text{Gy})\downarrow$	0.713±0.387	1.115±0.420	0.620±0.299	0.844±0.332	1.038±0.385	<b>0.328±0.261</b>
	$\Delta V_{95}(\%) \downarrow$	0.377±0.301	0.562±0.463	0.495±0.448	0.593±0.462	0.582±0.456	<b>0.201±0.214</b>
Heart	$\Delta D_{mean}(\text{Gy})\downarrow$	1.289±1.408	1.120±1.454	1.503±1.802	0.996±1.330	1.293±1.596	<b>0.938±1.061</b>
	$\Delta V_{30}(\%) \downarrow$	1.679±2.541	2.021±3.549	2.094±3.775	1.081±1.810	2.026±3.645	<b>1.315±2.026</b>
Ipsilateral	$\Delta D_{mean}(\text{Gy})\downarrow$	1.179±0.986	0.910±0.704	1.491±1.069	1.071±0.787	1.105±0.927	<b>0.872±0.737</b>
lung	$\Delta V_{20}(\%) \downarrow$	1.566±1.465	1.709±1.269	1.772±1.695	2.092±1.325	1.868±1.246	<b>1.345±1.021</b>
Spinal cord	$\Delta D_{max}(\text{Gy})\downarrow$	1.037±1.050	1.376±1.317	1.557±1.273	1.183±1.018	1.238±1.284	<b>0.877±0.812</b>

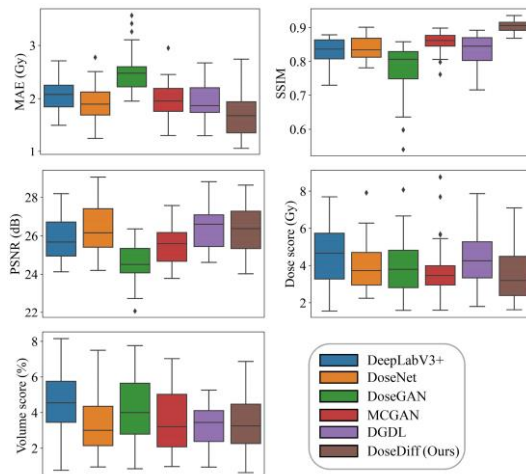


**Fig. 7.** Quantitative comparison with SOTA methods for dose prediction on NPC dataset.

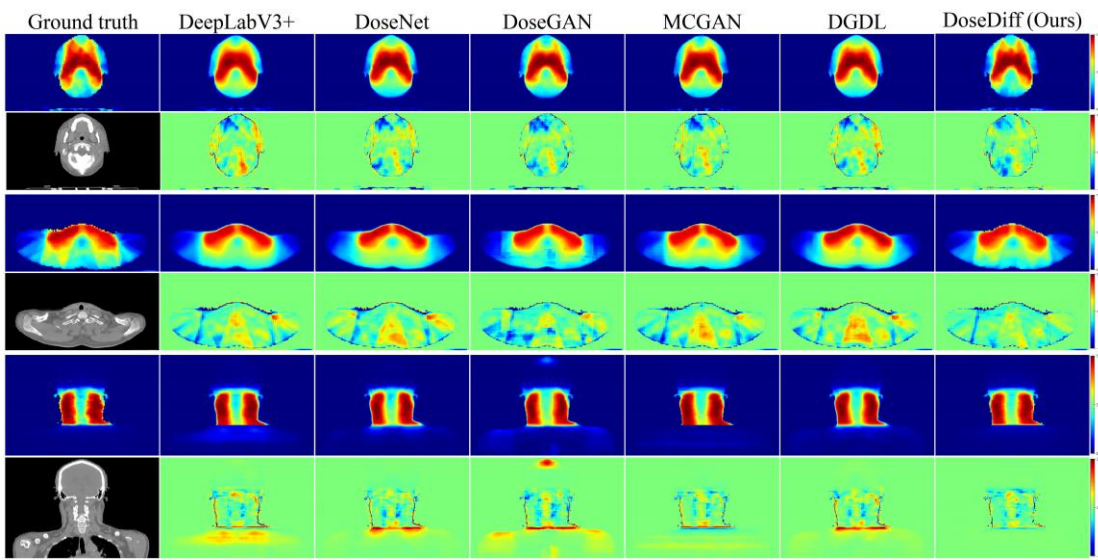


**Fig. 8.** Visual comparison of predicted dose distribution maps from different methods on the NPC dataset.

**Comparison on NPC dataset:** Fig. 7 presents the results of a quantitative

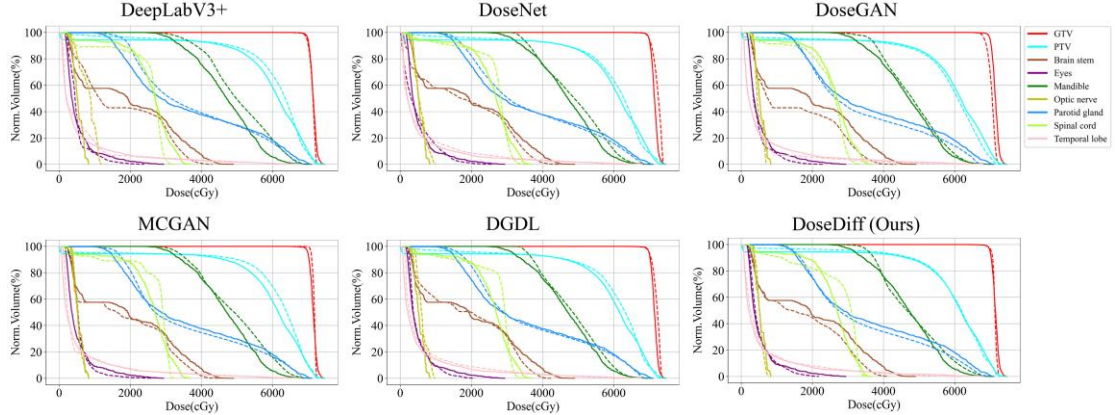


**Fig. 9.** The dose-volume histograms (DVHs) of the dose distribution maps predicted by the different methods on a testing NPC patient. The solid line represents the ground-truth DVH, while the dotted line represents the DVH of the predicted dose distribution map.

comparison between our method and the SOTA approaches on the NPC dataset. The experiments demonstrate that our method achieves competitive results in terms of both image similarity and dosimetry-related metrics. The transverse and coronal plane samples of dose distribution maps predicted by all the compared methods are shown in Fig. 8. Similar to the performance observed on the breast cancer dataset, we can observe that the dose distribution maps predicted by previous methods are overly smooth, while our method's predictions retain more realistic ray path characteristics. Furthermore, we can observe from the coronal images that our method maintains a high level of prediction accuracy for regions that are far away from the ROIs, thanks to the distance information provided by the PSDM. The DVH curves of the dose distribution maps predicted by the compared methods on the NPC dataset are presented in Fig. 9. Compared to other methods, the DVH curves of the target and OARs predicted by our method are closer to the ground truth.

### 3.7 The influence of non-deterministic prediction

Every dose prediction in our DoseDiff begins with a randomly generated Gaussian noise image. Moreover, each step in the DDIM-based inverse process involves Gaussian sampling as in Eqs. (7) and (8). The randomness introduced by these two factors leads to the non-determinism in dose prediction of our model. To investigate the influence of this non-determinism on the prediction results, we conducted 50 dose predictions for both breast cancer and NPC datasets using different random seeds. The variance of each mean metric for our DoseDiff on the two datasets are shown in Table 4, and the results indicate a small degree of fluctuation for each metric.

**Table 4** The variance of each mean metric for our DoseDiff with 50 different Gaussian samplings on the two datasets.

Dataset	MAE	SSIM	PSNR	Dose score	Volume score
Breast cancer	$\pm 0.0011$	$\pm 0.0002$	$\pm 0.0099$	$\pm 0.0058$	$\pm 0.0029$
NPC	$\pm 0.0012$	$\pm 0.0001$	$\pm 0.0076$	$\pm 0.0226$	$\pm 0.0153$

## 4 Discussion

In this study, we aim to develop a model to accurately predict dose distribution for each RT patient, so the medical physicist can achieve an acceptable radiotherapy plan with less trial and error. Clinically, both CT images and ROI masks are essential for radiotherapy planning, so most previous studies use deep learning to directly learn the mapping from them to dose distribution maps. However, the image of mask prevents the deep learning model from effectively extracting distance information between surrounding tissues and the targets or OARs. Some studies have replaced masks with distance maps and improved dose prediction accuracy [19, 23] because each voxel of the distance map explicitly provides the distance information relative to the ROI contour. Besides, inspired by the success of the diffusion model, we propose a distance-aware conditional diffusion model called DoseDiff for dose prediction. While using the distance maps as input, we also explore the fusion strategy of distance maps and CT images. We incorporate multi-scale fusion strategy and fusionFormer module into the proposed MMFNet to achieve effective fusion of complex information.

The diffusion model naturally possesses a strong ability to model data distributions, as it was specifically developed for this purpose. Therefore, one advantage of introducing conditional diffusion model into the image-to-image translation tasks is that conditional diffusion model can not only learn the mapping relationship from conditions to output but also effectively capture the distribution characteristics of the generated image itself. In contrast, previous methods only learned the mapping relationship between input and output images. Figures 5 and 8 demonstrate that the dose distribution maps generated by our method are more realistic. On the contrary, the ray path characteristics in the dose distribution maps generated by the previous method are unclear and distorted. These dose distribution maps may not exist in the real world and may be limited in their usefulness for assisting medical physicists in obtaining the relevant parameters for treatment planning.

Unlike the previous single-step methods, conditional diffusion model predicts the dose distribution through a multi-step denoising process. This paradigm progressively recovers prediction results from Gaussian noise in a recursive manner, which improves the reliability and realism of the results. Table 1 shows that conditional diffusion model outperforms the single-step UNet model in various metrics on dose prediction. However, the multi-step paradigm inevitably increases the time for model training and inference. We explore the relationship between the performance and inference time of the DoseDiff at different diffusion steps in Section 3.5. Utilizing DDIM technology, the experimental results have demonstrated that our DoseDiff is able to generate an accurate dose distribution map for a new patient in only 8 steps.

Proper use of distance maps is able to improve the performance of dose prediction models. The unit distance in the vanilla SDM (i.e., MSDM) is one voxel, so the magnitude of the values in MSDM is usually comparable to the volume size. Such large values are usually not conducive to the stable training of neural networks. Therefore, Yue et al. [23] proposed a voxel-wise transformation to shrink the value in SDM. The transformation keeps the value inside the ROI large, while gradually decreasing the

value outside the ROI that eventually approaches zero, which makes the numerical distribution trend in SDM similar to that of the dose distribution. However, this transformation is too drastic, which causes a large number of voxels outside ROI to become zero, rendering them unable to provide effective distance information. Our experiments demonstrate that the MSDM simply divided by a normalization constant achieves better performance than TSBDM, as shown in Table 2. The PSDM can be regarded as a global normalized version of MSDM with the introduction of spacing information. The transformation in TSBDM is still the instance-wise normalization, while our proposed PSDM normalizes the values in all SDM to a unified distance unit (e.g., decimetre). Therefore, the model can extract and analyze the information in PSDM more efficiently. In addition, PSDM is calculated in 3D volume, so every voxel in PSDM contains certain 3D information. Although our DoseDiff is a 2D model, with the support of PSDM, its performance is not inferior to SOTA 3D models (i.e., DoseNet, DoseGAN, and DGDL).

The existing dose prediction methods usually adopt early fusion for CT image and mask/SDM, i.e., concatenating them at the input level. This fusion strategy is easy to implement, but often suboptimal. Therefore, we propose MMFNet to extract more valuable interactive information between CT image and PSDM. The MMFNet adopts multi-scale feature-level fusion for CT image and PSDM. Moreover, a fusionFormer module is used to perceive long-range dependence and global information fusion. Long-range perception is important for dose prediction because the dose of a voxel is related to all the tissues through which the ray passes before reaching that voxel. Transformer has better long-range perception capability compared to CNN, so we designed this transformer-based fusion module. The experimental results in Table 1 show the effectiveness of our fusion strategy.

There are several limitations in our work. First, the 3D information provided by PSDM is relatively limited. Our method is unable to use the 3D structural information of CT images, which is beneficial to dose prediction. Therefore, our future work will focus on expanding the DoseDiff into a 3D model. Second, the DoseDiff has no advantage in inference speed compared with the one-step dose prediction models. The paradigm of diffusion model inevitably incurs more inference costs. Fortunately, some approaches, e.g., DDIM, have been proposed to reduce the inference time of diffusion model and preserve the model performance. Third, while non-deterministic predictions have limited influence on model performance as shown in Table 4, they remain an unresolved issue that requires attention. This is a common challenge for applying conditional diffusion model to image-to-image tasks.

## 5 Conclusion

In this paper, we propose the DoseDiff, a distance-aware conditional diffusion model, for predicting dose distribution maps. The DoseDiff uses the CT images and SDMs as conditions and dose distribution map prediction is defined as a sequence of denoising steps guided by these conditions. Using PSDM as a model input achieves better performance compared to using a mask, as it can effectively provide distance

information. Moreover, the MMFNet is proposed to effectively extract and fuse features from CT images and SDMs. Ablation studies evaluated the contribution of each element in our DoseDiff. Comparison results with other methods on two datasets showed that our DoseDiff achieves state-of-the-art performance in dose prediction.

## References

1. Sahiner, B., et al., *Deep learning in medical imaging and radiation therapy*. 2019. **46**(1): p. e1-e36.
2. Delaney, G., et al., *The role of radiotherapy in cancer treatment: estimating optimal utilization from a review of evidence-based clinical guidelines*. 2005. **104**(6): p. 1129-1137.
3. Craft, D.L., et al., *Improved planning time and plan quality through multicriteria optimization for intensity-modulated radiotherapy*. 2012. **82**(1): p. e83-e90.
4. Schreiner, L.J.J.o.m.p.A.o.M.P.o.l., *On the quality assurance and verification of modern radiation therapy treatment*. 2011. **36**(4): p. 189.
5. Zhan, B., et al., *Multi-constraint generative adversarial network for dose prediction in radiotherapy*. 2022. **77**: p. 102339.
6. Song, Y., et al., *Dose prediction using a deep neural network for accelerated planning of rectal cancer radiotherapy*. 2020. **149**: p. 111-116.
7. Shiraishi, S., et al., *Knowledge-based prediction of plan quality metrics in intracranial stereotactic radiosurgery*. 2015. **42**(2): p. 908-917.
8. Nwankwo, O., et al., *Knowledge-based radiation therapy (KBRT) treatment planning versus planning by experts: validation of a KBRT algorithm for prostate cancer treatment planning*. 2015. **10**(1): p. 1-5.
9. Wu, B., et al., *Data-driven approach to generating achievable dose-volume histogram objectives in intensity-modulated radiotherapy planning*. 2011. **79**(4): p. 1241-1247.
10. Song, T., et al., *Patient-specific dosimetric endpoints based treatment plan quality control in radiotherapy*. 2015. **60**(21): p. 8213.
11. Deshpande, R.R., et al., *Knowledge-driven decision support for assessing dose distributions in radiation therapy of head and neck cancer*. 2016. **11**: p. 2071-2083.
12. Valdes, G., et al., *Clinical decision support of radiotherapy treatment planning: A data-driven machine learning strategy for patient-specific dosimetric decision making*. 2017. **125**(3): p. 392-397.
13. Zhang, H.H., et al., *The minimum knowledge base for predicting organ-at-risk dose-volume levels and plan-related complications in IMRT planning*. 2010. **55**(7): p. 1935.
14. Morin, O., et al., *A deep look into the future of quantitative imaging in oncology: a statement of working principles and proposal for change*. 2018. **102**(4): p. 1074-1082.
15. Dong, P., L.J.P.i.M. Xing, and Biology, *Deep DoseNet: a deep neural network for accurate dosimetric transformation between different spatial resolutions and/or different dose calculation algorithms for precision radiation therapy*. 2020. **65**(3): p. 035010.
16. Fan, J., et al., *Automatic treatment planning based on three-dimensional dose distribution predicted from deep learning technique*. 2019. **46**(1): p. 370-381.
17. Kearney, V., et al., *DoseNet: a volumetric dose prediction algorithm using 3D fully-convolutional neural networks*. 2018. **63**(23): p. 235022.

18. Kearney, V., et al., *DoseGAN: a generative adversarial network for synthetic dose prediction using attention-gated discrimination and generation*. 2020. **10**(1): p. 11073.
19. Kontaxis, C., et al., *DeepDose: towards a fast dose calculation engine for radiation therapy using deep learning*. 2020. **65**(7): p. 075013.
20. Nguyen, D., et al., *3D radiotherapy dose prediction on head and neck cancer patients with a hierarchically densely connected U-net deep learning architecture*. 2019. **64**(6): p. 065020.
21. Nguyen, D., et al., *A feasibility study for predicting optimal radiation therapy dose distributions of prostate cancer patients from patient anatomy using deep learning*. 2019. **9**(1): p. 1076.
22. Sumida, I., et al., *A convolution neural network for higher resolution dose prediction in prostate volumetric modulated arc therapy*. 2020. **72**: p. 88-95.
23. Yue, M., et al., *Dose prediction via distance-guided deep learning: Initial development for nasopharyngeal carcinoma radiotherapy*. 2022. **170**: p. 198-204.
24. Hu, J., et al., *Incorporating historical sub-optimal deep neural networks for dose prediction in radiotherapy*. 2021. **67**: p. 101886.
25. Yuan, L., et al., *Quantitative analysis of the factors which affect the interpatient organ-at-risk dose sparing variation in IMRT plans*. 2012. **39**(11): p. 6868-6878.
26. Zhou, T., S. Ruan, and S.J.A. Canu, *A review: Deep learning for medical image segmentation using multi-modality fusion*. 2019. **3**: p. 100004.
27. Suk, H.-I., et al., *Hierarchical feature representation and multimodal fusion with deep learning for AD/MCI diagnosis*. 2014. **101**: p. 569-582.
28. Xie, L., et al., *CNTSeg: A multimodal deep-learning-based network for cranial nerves tract segmentation*. 2023. **86**: p. 102766.
29. Gulrajani, I., et al., *Improved training of wasserstein gans*. 2017. **30**.
30. Metz, L., et al., *Unrolled generative adversarial networks*. 2016.
31. Saharia, C., et al. *Palette: Image-to-image diffusion models*. in *ACM SIGGRAPH 2022 Conference Proceedings*. 2022.
32. Ho, J., A. Jain, and P. Abbeel, *Denoising diffusion probabilistic models*. *Advances in Neural Information Processing Systems*, 2020. **33**: p. 6840-6851.
33. Song, Y., et al., *Score-based generative modeling through stochastic differential equations*. 2020.
34. Dhariwal, P. and A.J.A.i.N.I.P.S. Nichol, *Diffusion models beat gans on image synthesis*. 2021. **34**: p. 8780-8794.
35. Lugmayr, A., et al. *Repaint: Inpainting using denoising diffusion probabilistic models*. in *Proceedings of the IEEE/CVF Conference on Computer Vision and Pattern Recognition*. 2022.
36. Saharia, C., et al., *Image super-resolution via iterative refinement*. *IEEE Transactions on Pattern Analysis Machine Intelligence*, 2022.
37. Cai, L., H. Gao, and S. Ji. *Multi-stage variational auto-encoders for recursive image generation*. in *Proceedings of the 2019 SIAM International Conference on Data Mining*. 2019. SIAM.
38. Ma, Y., et al. *Coarse-to-Fine Image Inpainting via Region-wise Convolutions and Non-Local Correlation*. in *IJCAI*. 2019.

39. Lei, J., et al., *C2FNet: A Coarse-to-Fine Network for Multi-View 3D Point Cloud Generation*. 2022. **31**: p. 6707-6718.
40. Vaswani, A., et al., *Attention is all you need*. 2017. **30**.
41. Dosovitskiy, A., et al., *An image is worth 16x16 words: Transformers for image recognition at scale*. 2020.
42. Ho, J., A. Jain, and P.J.A.i.N.I.P.S. Abbeel, *Denoising diffusion probabilistic models*. 2020. **33**: p. 6840-6851.
43. Nichol, A.Q. and P. Dhariwal. *Improved denoising diffusion probabilistic models*. in *International Conference on Machine Learning*. 2021. PMLR.
44. Luo, C.J.a.p.a., *Understanding diffusion models: A unified perspective*. 2022.
45. Song, J., C. Meng, and S.J.a.p.a. Ermon, *Denoising diffusion implicit models*. 2020.
46. d'Ascoli, S., et al. *Convit: Improving vision transformers with soft convolutional inductive biases*. in *International Conference on Machine Learning*. 2021. PMLR.
47. Yuan, K., et al. *Incorporating convolution designs into visual transformers*. in *Proceedings of the IEEE/CVF International Conference on Computer Vision*. 2021.
48. Xie, Y., et al. *Cotr: Efficiently bridging cnn and transformer for 3d medical image segmentation*. in *Medical Image Computing and Computer Assisted Intervention–MICCAI 2021: 24th International Conference, Strasbourg, France, September 27–October 1, 2021, Proceedings, Part III* 24. 2021. Springer.
49. Loshchilov, I. and F.J.a.p.a. Hutter, *Decoupled weight decay regularization*. 2017.
50. Wang, Z., et al., *Image quality assessment: from error visibility to structural similarity*. 2004. **13**(4): p. 600-612.